Advances in Aircraft and Spacecraft Science, *Vol. 9, No. 5 (2022) 415-431*
https://doi.org/10.12989/aas.2022.9.5.415

RANS simulation of secondary flows in a low pressure turbine cascade: Influence of inlet boundary layer profile

Michele Errante*, Andrea Ferrero[a] and Francesco Larocca[b]

Department of Mechanical and Aerospace Engineering, Politecnico di Torino, Corso Duca degli Abruzzi 24, 10129 Torino, Italy

(Received December 29, 2021, Revised August 9, 2022, Accepted September 2, 2022)

Abstract. Secondary flows have a huge impact on losses generation in modern low pressure gas turbines (LPTs). At design point, the interaction of the blade profile with the end-wall boundary layer is responsible for up to 40% of total losses. Therefore, predicting accurately the end-wall flow field in a LPT is extremely important in the industrial design phase. Since the inlet boundary layer profile is one of the factors which most affects the evolution of secondary flows, the first main objective of the present work is to investigate the impact of two different inlet conditions on the end-wall flow field of the T106A, a well known LPT cascade. The first condition, labeled in the paper as C1, is represented by uniform conditions at the inlet plane and the second, C2, by a flow characterized by a defined inlet boundary layer profile. The code used for the simulations is based on the Discontinuous Galerkin (DG) formulation and solves the Reynolds-averaged Navier-Stokes (RANS) equations coupled with the Spalart Allmaras turbulence model. Secondly, this work aims at estimating the influence of viscosity and turbulence on the T106A end-wall flow field. In order to do so, RANS results are compared with those obtained from an inviscid simulation with a prescribed inlet total pressure profile, which mimics a boundary layer. A comparison between C1 and C2 results highlights an influence of secondary flows on the flow field up to a significant distance from the end-wall. In particular, the C2 end-wall flow field appears to be characterized by greater over turning and under turning angles and higher total pressure losses. Furthermore, the C2 simulated flow field shows good agreement with experimental and numerical data available in literature. The C2 and inviscid Euler computed flow fields, although globally comparable, present evident differences. The cascade passage simulated with inviscid flow is mainly dominated by a single large and homogeneous vortex structure, less stretched in the spanwise direction and closer to the end-wall than vortical structures computed by compressible flow simulation. It is reasonable, then, asserting that for the chosen test case a great part of the secondary flows details is strongly dependent on viscous phenomena and turbulence.

Keywords: boundary layer development; Computational Fluid Dynamics (CFD); discontinuous Galerkin; low pressure turbine cascade; secondary flows

1. Introduction

The influence of secondary flows on the flow field in modern gas turbines is an issue of paramount importance. In low-pressure turbines (LPTs) the set of complex three-dimensional

*Corresponding author, Ph.D. Student, E-mail: michele.errante@polito.it
[a]Assistant Professor, E-mail: andrea_ferrero@polito.it
[b]Professor, E-mail: francesco.larocca@polito.it

http://www.techno-press.org/?journal=aas&subpage=7 ISSN: 2287-528X (Print), 2287-5271 (Online)

vortex structures, originated from the interaction between the incoming end-wall boundary layer and the cascade, is responsible for a significant fraction of total losses.

Over the years, many authors have shed light on the nature of secondary flows. The review works carried out by Sieverding (1985), Langston (2001) were crucial in summarizing the general flow topology of the vortex system generated by secondary flows. As reported by Langston (1980), peculiar of that vortex system is the inlet boundary layer separation upstream of the leading edge due to the potential flow field induced by the blade, which provokes the formation of a horseshoe vortex (HP) with two legs stretching along the suction and pressure side of the blade. Due to the passage pressure-to-suction end-wall flow (crossflow), driven by the pressure difference between the suction and pressure side of two adjacent blades, the pressure-side leg of the horseshoe vortex is forced to move away from the pressure side toward the suction side after it enters the passage, feeding the passage vortex (PV), with which it shares the same sense of rotation. The behavior of the other leg of the horseshoe vortex (suction side leg) has not been uniquely described in literature. Sieverding and Van Den Bosche (1983), Wang *et al.* (1997) observed that the suction leg wraps around the passage vortex through the passage. Conversely, in the model proposed by Goldstein and Spores (1988) it moves upward on the suction surface. And additional vortex has been recognized in several studies among the aerodynamic structures that constitute the secondary flows, named counter vortex (CV) and located above the passage vortex, counter-rotating with respect to it.

The present study, which is an extension of a previous investigation (Errante *et al.* 2022), has a twofold purpose. Firstly, since it is known that one of the factors which most affects the end-wall flow field in a low pressure turbine cascade is the incoming boundary layer state (de la Blanco *et al.* 2003, Cui *et al.* 2017), this work aims to assess the differences in the T106A turbine cascade secondary flows structures comparing a case in which perfectly uniform conditions are set at the inlet to a case in which a well defined boundary layer is imposed at the inlet. The code used for the simulations is based on the Discontinuous Galerkin (DG) formulation and solves the Reynolds Averaged Navier-Stokes (RANS) equations coupled with the Spalart Allmaras turbulence model.

As mentioned at the beginning of the present introduction, the horseshoe vortex generation is an inviscid mechanism. It occurs upstream of any bluff body placed orthogonally to an end-wall on which a boundary layer profile has developed. The secondary flows pattern is the result of the modification of the horseshoe vortex by the viscosity, turbulence and the geometry of the cascade. For this reason, the present study, as second main objective, attempts to provide an estimation of the influence of viscosity and turbulence on the T106A end-wall flow field through a comparison between the boundary layer RANS results and those obtained from a further simulation performed by solving the inviscid Euler equations, imposing equal inlet conditions.

2. Test case description

The current study aims to investigate, by means of Reynolds Averaged Navier-Stokes (RANS) analysis the end-wall flow field in the T106A linear low pressure turbine (LPT) cascade. This highly loaded LPT cascade is characterized by a pitch t to axial chord c_x ratio equal to $t/c = 0.929$ and an inlet flow angle β_s equal to $37.7°$ with respect to the axial direction. In accordance to the measurements undertaken by Duden and Fottner (1997) and to the numerical works carried out by Pichler *et al.* (2019), Marconcini *et al.* (2019), the isentropic exit Mach $M_{2,is}$ and the isentropic exit Reynolds number $Re_{2,is}$ were set equal to $M_{2,is} = 0.59$ and $Re_{2,is} = 120000$, respectively.

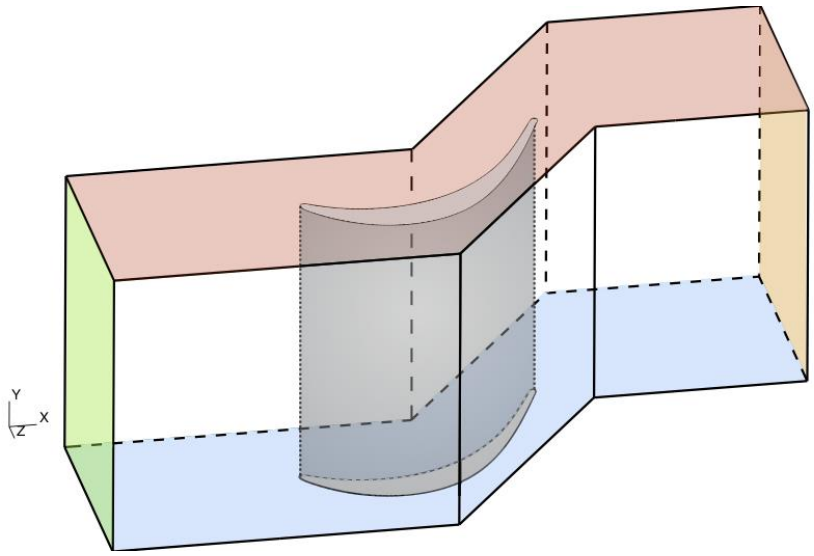

Fig. 1 Computational domain. The inlet and outlet planes are marked in green and orange respectively, while the midspan surface and the end-wall are colored blue and red, respectively

In Fig. 1 is shown the computational domain built for the RANS and Euler analyses, where x,y and z are the axial, spanwise and pitchwise directions, respectively. Since the calculations were carried out using non-dimensional quantities, all geometric specifications were scaled with respect to the axial chord c_x. The leading edge was located at $x = 0$, the inlet at $x = -0.8\, c_x$ and the outlet at $x = 2\, c_x$, hence the total axial extension of the domain was set equal to 2.8 times the blade axial chord. The span H to axial chord c_x ratio was fixed equal to $H/c_x = 2.206$, and since the flow field was expected to be symmetrical with respect to the midspan plane, the spanwise extension of the domain was set exactly equal to half of the span dimension, which means that the end-wall surface was positioned at $y = 1.1029\, c_x$. While for Euler simulation the inviscid wall boundary condition was imposed both at the midspan plane and at the end-wall, for RANS adiabatic boundary condition and inviscid wall boundary condition were imposed at the end-wall and midspan plane, respectively. In order to simulate a linear cascade, periodic boundary conditions were used to connect the faces located at the pitchwise domain boundary.

As mentioned above, RANS computations were conducted for two different cases which differ in terms of inlet conditions. The first one, which will be referred to as C1, was obtained imposing uniform conditions on the inlet section. For the second case C2, an end-wall boundary layer profile reconstructed from the data available from Duden and Fottner (1997), Pichler *et al.* (2019) was set on the inlet section. The same boundary layer profile employed in C2 was also used for the simulation in which the Euler equations were solved.

The axial velocity u profile at the inlet is displayed in Fig. 2(a) and the values of boundary layer thickness δ, displacement thickness δ^* and momentum thickness θ referred to the axial chord c_x at inlet are shown in Table 1 together with the parameters of the experimental work conducted by Duden and Fottner (1997). In order to ensure the desired inlet boundary layer for C2 and Euler computations, the total pressure p° and total temperature T° shown in Figs. 2(b)-(c) were imposed as inlet boundary conditions. Furthermore, as will be mentioned below, since the Spalart-Allmaras (SA) turbulence model (Allmaras *et al.* 2012) was the closure model chosen for

Table 1 Inlet boundary layer parameters

	C2 & Euler	Duden and Fottner (1997)
δ/c_x	0.3014	0.3005
δ^*/c_x	0.0452	0.0305
θ/c_x	0.0332	0.0332

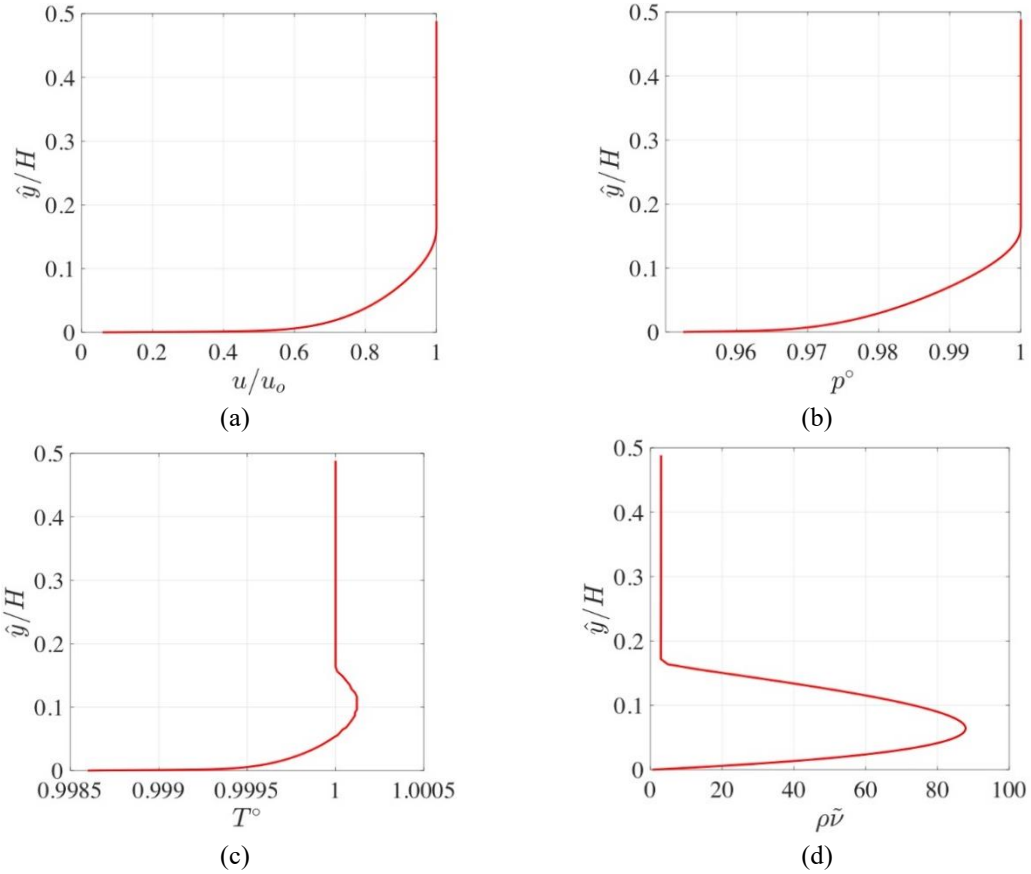

Fig. 2 Inlet spanwise distributions of (a) the axial component of velocity u, (b) total pressure p°, (c) total temperature T° and (d) modified eddy viscosity $\tilde{\nu}$, where $\hat{y}$ is the distance from the end-wall, H is the span dimension, u_0 is axial velocity at the midspan plane and ρ is the density

the RANS equations, for C2 was required to set the modified eddy viscosity (or Spalart Allmaras variable) $\tilde{\nu}$ as additional inlet boundary condition. The modified eddy viscosity $\tilde{\nu}$ profile multiplied by density ρ is illustrated in Fig. 2(d).

3. Numerical method

The simulations were performed by means of a research code, developed at the Department of Mechanical and Aerospace Engineering (DIMEAS) of Politecnico di Torino, which solves the

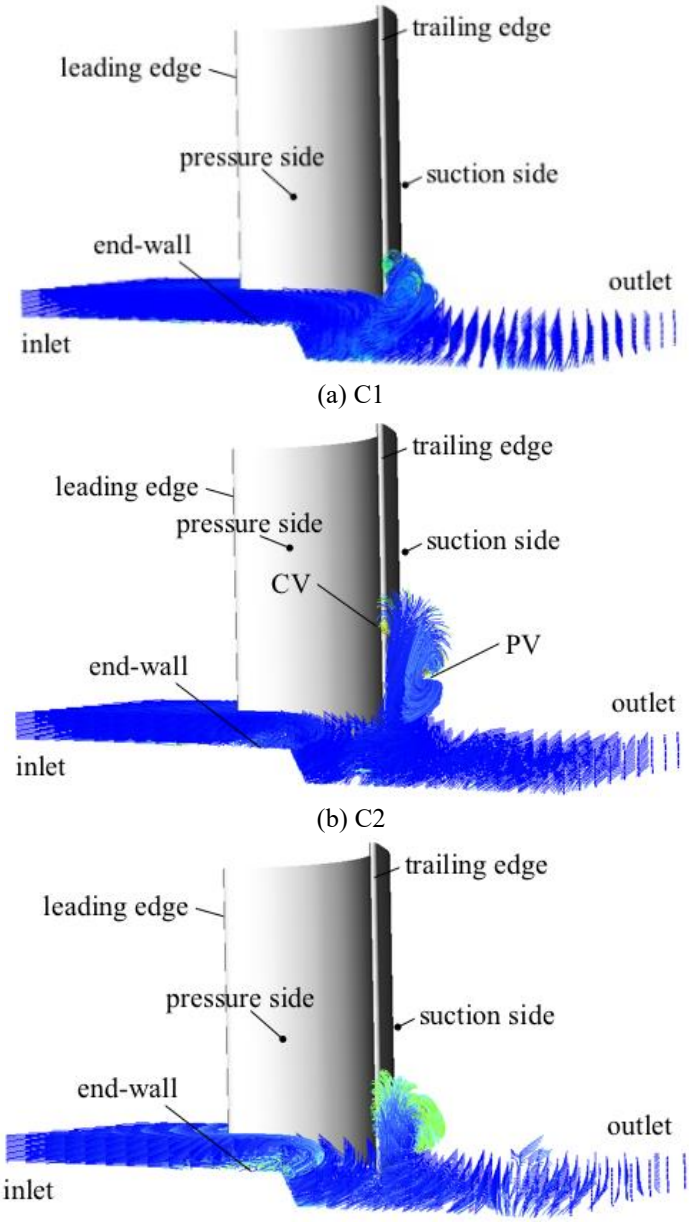

Fig. 3 End-wall flow streamlines within the cascade passage. The view plane is located downstream of the passage. The inlet and the outlet of the passage, the leading edge, the trailing edge, the suction and the pressure sides of the blade and the end-wall are indicated for clarity. For C2, the passage vortex (PV) and the counter vortex (CV) are highlighted

unsteady, three-dimensional, Reynolds-averaged Navier-Stokes equations (for C1 and C2) and Euler equations in a finite elements framework, based on the Discontinuous Galerkin (DG) formulation. In the last decade, unstructured finite element high-order methods such as the

discontinuous Galerkin method have been proven able to combine high accuracy to the flexibility offered by unstructured body fitted meshes or embedded methods (Giuliani 2022, Gulizzi 2022). In particular, Ghidoni *et al.* (2013) investigated the flow field in T106A turbine cascade far from the end-wall by a high-order accurate DG space discretization method with implicit time integration solving the RANS equations coupled with the $k-\omega$ turbulence model, showing accurate results on very coarse grids. Garai *et al.* (2017) demonstrated that the DG method can capture the high Reynolds number flow-field in a High Pressure turbine (HPT) configuration and Yao and He (2019) showed good results by solving RANS equation to describe the end-wall flow field in a high-pressure turbine cascade using the discontinuous Galerkin discretization on unstructured mesh.

For RANS simulations of the present work, convective fluxes are discretized by means of an approximate Riemann problem solver implemented according to Pandolfi (1984), while for Euler simulation the local Lax-Friedrichs (Lax 1954, Leveque 2002) or Rusanov (1962) flux is used. The Enhanced Stability Recovery (ESR) approach proposed by Ferrero *et al.* (2015) is adopted for computing diffusive fluxes. The recovery scheme, originally proposed by Lo and van Leer (1985), allows to obtain a smooth differentiable function at the interface between two elements which has to be equivalent in the weak sense to the original solution on the two elements. The ESR scheme shows a larger stability limit with respect to the original recovery scheme and the discretized equations remain well conditioned even in the presence of highly distorted meshes. As already mentioned above, the closure model adopted for the RANS equations was the Spalart-Allmaras (SA) turbulence model, in the version described by Allmaras *et al.* (2012). The scheme selected for computations is second order accurate in space and for time discretization the implicit backward Euler scheme was used in order to get the steady solution by time-marching. The linear system obtained by the implicit discretization is solved in parallel by means of the GMRES method with the additive Schwarz preconditioner implemented in PetsC library (Balay *et al.* 1997). The same library is also used to manage the unstructured mesh in the parallel environment. The grid was generated by the open-source Gmsh software (Geuzaine and Remacle 2009), using a multi-block grid assembled by an O-type structured grid around the blade profile and a unstructured grid for the external domain, for a total of about 2.4 million hexahedra. Since a second order accurate DG scheme was used for RANS, each element is characterized by 4 degrees of freedom (DOFs) and so the total number of DOFs per equation for C1 and C2 is approximately equal to 9.6 million. Particular attention was paid to the size of elements close to the blade and in proximity of the end-wall, to ensure adequate spatial resolution for both the boundary layer and aerodynamic structures constituting the secondary flows. No convergence study is reported in the present work because this issue was investigated in previous works on this cascade and so the mesh resolution was chosen according to previous experiences.

4. Results

4.1 Streamlines

The most immediate way to visualize the aerodynamic structures constituting the secondary flows is to observe the streamlines within the cascade passage. In Fig. 3 are shown the streamlines in the end-wall proximity. In particular, are included in the visualization only the streamlines crossing the inlet plane at a distance from the end-wall of 9% of the spanwise domain dimension

(about 4% of the entire blade span length). In illustrations displayed in Fig. 3 the view plane is located downstream of the passage, from which it is possible to notice that most of the vortex activity is relegated to the suction side, where it is clearly visible the passage vortex and the counter vortex. Making a comparison between C1 and C2, it is evident that the boundary layer present at the C2 inlet leads to a greater dimension of the secondary flows aerodynamic structures. Streamlines in C2, crossing the inlet plane at a distance from the end-wall of 9% of the spanwise domain dimension, further cross a plane located downstream of the trailing edge at a distance from the end-wall of more than 50% of the spanwise domain extent, in contrast to those in C1, only reaching the 30%.

As mentioned above, since the origin of the horseshoe vortex does not depend on the presence of viscous effects, in Fig. 3(c) it is possible to see secondary flows streamlines obtained by solving Euler equations. Both pressure side and suction side legs appear more stretched in the pitchwise direction rather than the spanwise direction, crossing a plane downstream of the trailing edge at a distance from the end-wall of nearly 40% of the spanwise domain dimension.

4.2 Pressure distribution, C1 vs. C2

The evaluation of the pressure coefficient distribution c_p provides a very clear idea of the effects of secondary flows on the blade load variation along the span. It is defined as

$$c_p = \frac{p(x) - p_{out}}{p_{in}^{\circ} - p_{out}} \tag{1}$$

where p_{in}° is the freestream stagnation pressure at the inlet and p_{out} is the mass-average static pressure at the outlet.

With reference to Fig. 4, it can be seen that the presence of the inlet boundary layer for case C2 has a tangible influence close to the end-wall, where the pressure and suction sides curves get closer, narrowing the area between them. This is reflected in a reduction of lift generated by the blade as the end-wall is approached from midspan passing from C1 to C2. What has just been said can also be observed in Table 2 where the lift coefficient defined as

$$C_L = \frac{L}{\frac{1}{2}\rho V_{\infty}^2 (c_x \cdot 1)} = \int_0^1 \left(c_{p_p} - c_{p_s}\right) d\left(\frac{x}{c_x}\right) \tag{2}$$

is evaluated at different spanwise locations $\hat{y}/H$ for C1 and C2, indeed for 0% and 2% of the span, the lift coefficient C_L falls by 20% moving from C1 to C2. Furthermore, referring to the results at $\hat{y}/H = 0$, it can be observed that the C2 curve follows the experimental results presented by Duden and Fottner (1997) very well, especially up to 80% of the profile axial chord.

Table 2 Evolution of lift coefficient C_L along the blade span, comparison between C1 and C2 results

C_L (C1)	C_L (C2)	$\hat{y}/H$	Var. (%)
0.752	0.613	0	-18.49
0.846	0.671	0.02	-20.72
0.878	0.852	0.15	-3.067
0.884	0.894	0.5	+1.122

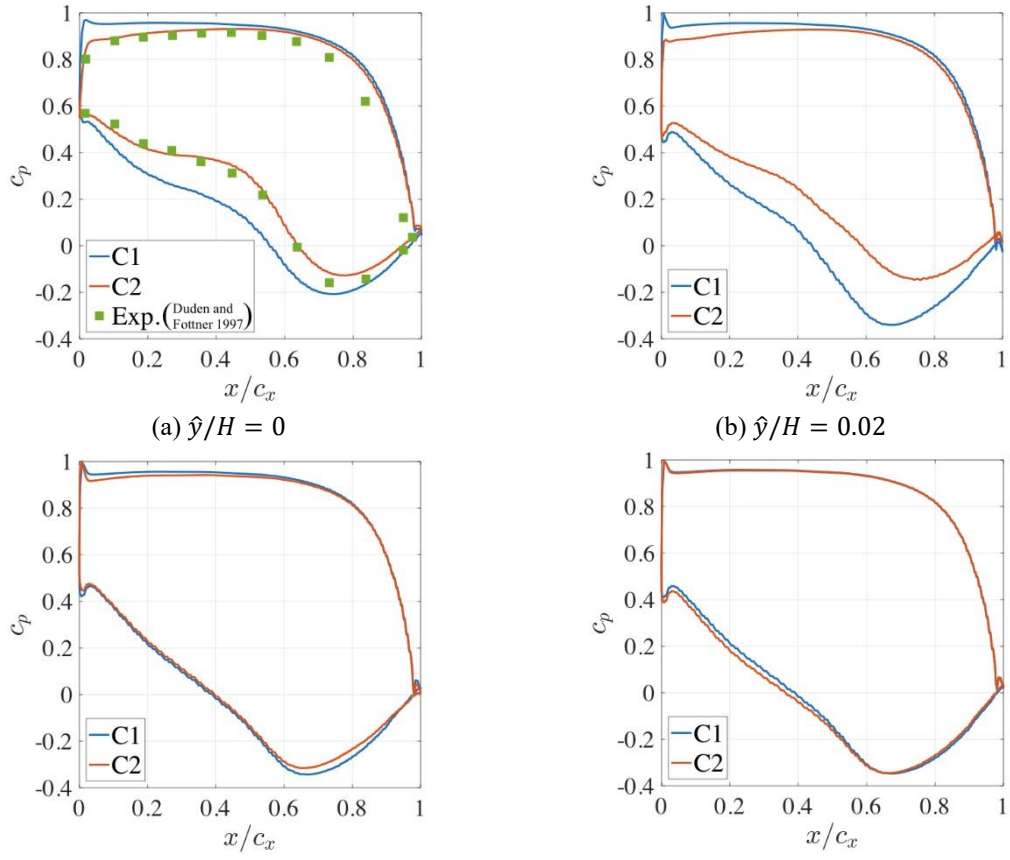

(a) $\hat{y}/H = 0$ (b) $\hat{y}/H = 0.02$

(c) $\hat{y}/H = 0.15$ (d) $\hat{y}/H = 0.50$

Fig. 4 Pressure distribution around the blade at different spanwise locations $\hat{y}/H$, where $\hat{y}$ is the distance from the end-wall and H is the span dimension. The experimental data by Duden and Fottner (1997) labeled as “Exp" and presented with squares, are only available at $\hat{y}/H = 0$

4.3 Flow angle evolution downstream of the blade trailing edge, C1 vs. C2

Fig. 5 illustrates the mass-averaged flow angle β evolution downstream of the blade trailing edge. The distance from the end-wall $\hat{y}$ divided by the span dimension H_1 used by Duden and Fottner (1997), approximately equal to 3.5 times the axial chord c_x, is reported on the ordinate axis, in order to make comparison with the experimental results possible. The peculiar pattern of a turbine cascade is visible: an overturning of the flow in proximity of the end-wall followed by an underturning as the distance from the midspan decreases.

By comparing the two cases, it can be seen that both over turning and under turning phenomena are more pronounced and shifted towards the midspan in C2 than in C1. The difference between the two under turning peaks, distant from each other by $\Delta y/c_x = 0.15$ in the spanwise direction, is approximately equal to $\Delta\beta = 2.5°$, which corresponds to a relative increase of 4% passing from uniform conditions to a boundary layer profile at the inlet. On the other hand, the deviation between the two over turning maxima rises as x/c_x increases to an approximate value of $\Delta\beta = 7°$

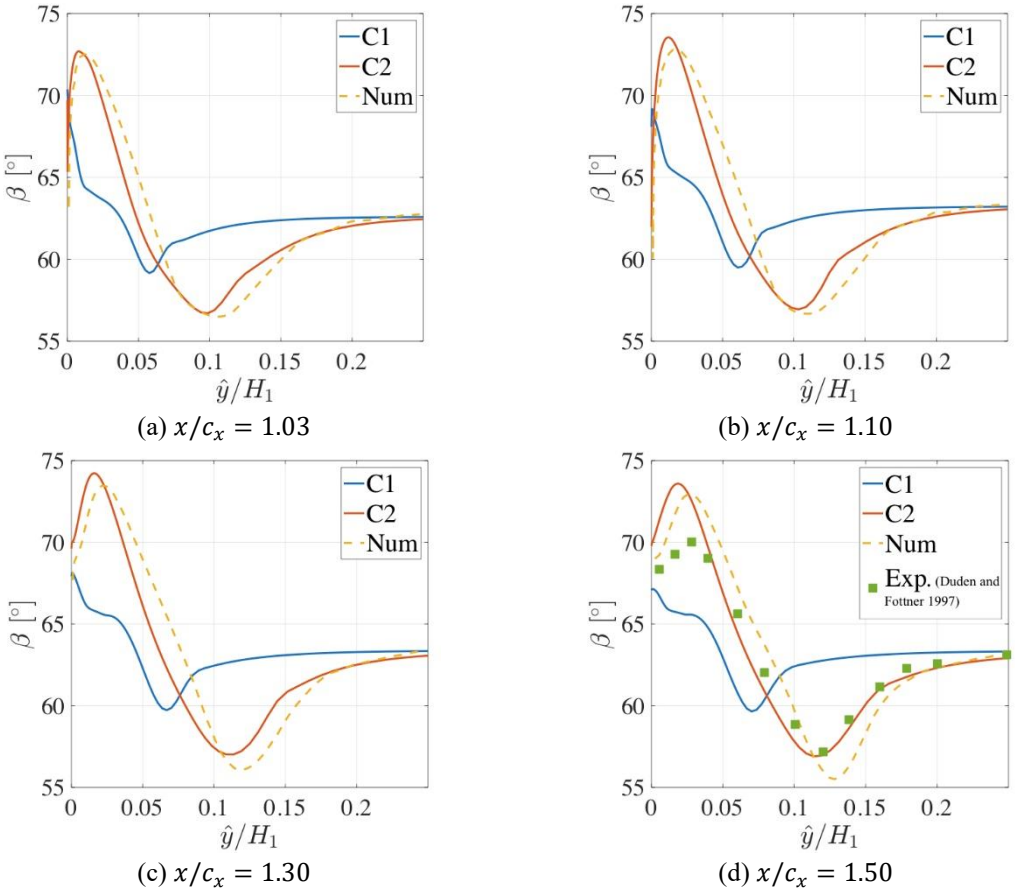

(a) $x/c_x = 1.03$ (b) $x/c_x = 1.10$

(c) $x/c_x = 1.30$ (d) $x/c_x = 1.50$

Fig. 5 Pitchwise averaged flow angle β with respect to the axial direction along the spanwise direction at four axial locations. The LES results by Pichler *et al.* (2019) labeled as "Num" are presented with dashed line and the Duden and Fottner (1997) experimental measurements labeled as "Exp", only available at $x/c_x = 1.50$, are presented with squares

for $x/c_x = 1.5$, corresponding to a relative increase of 10% in β by passing from C1 to C2. Furthermore, it can been observed that the data presented by Pichler *et al.* (2019), Duden and Fottner (1997) accurately follow the C2 curve pattern. The differences between the numerical results are most likely due to the different turbulence models and possibly different boundary layer profiles.

4.4 Loss generation, C1 vs. C2

The spanwise distributions of the total pressure loss coefficient ω at different axial locations downstream the trailing edge defined as

$$\omega = \frac{p_{in}^{\circ} - p^{\circ}}{p_{in}^{\circ} - p} \tag{3}$$

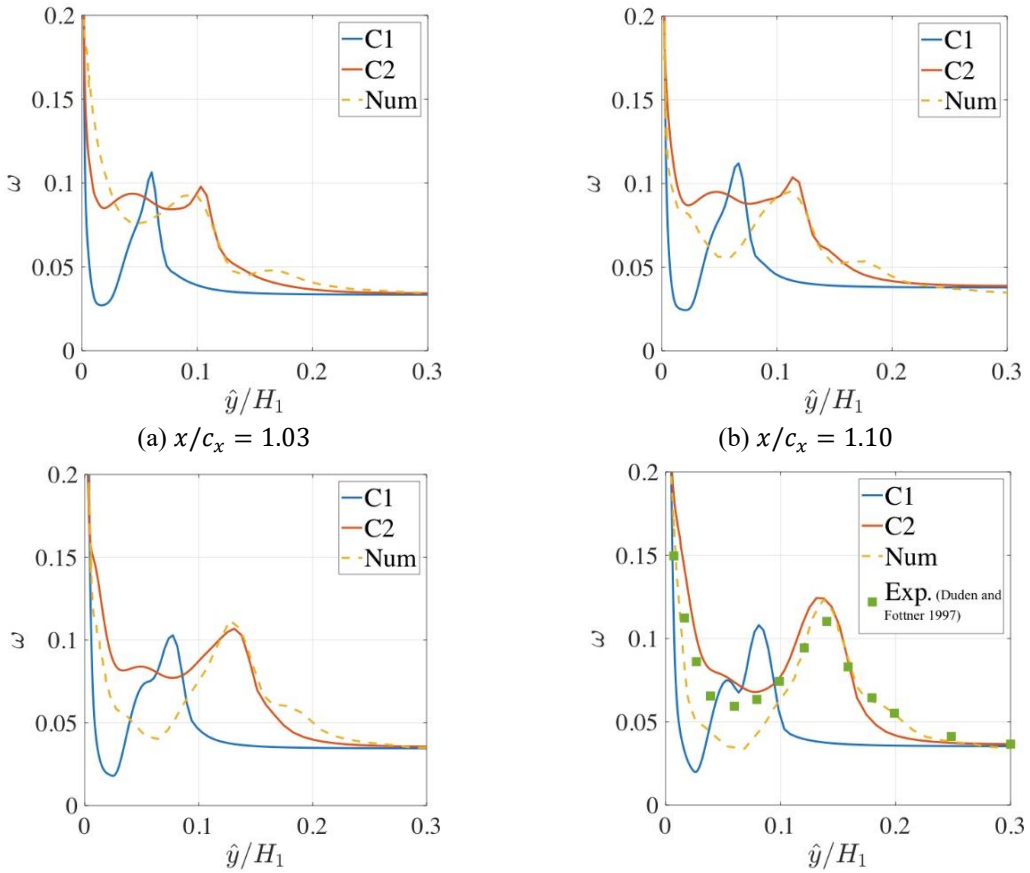

(a) $x/c_x = 1.03$ (b) $x/c_x = 1.10$

(c) $x/c_x = 1.30$ (d) $x/c_x = 1.50$

Fig. 6 Spanwise distributions of total pressure loss coefficient at four axial locations. The RANS results by Marconcini *et al.* (2019) labeled as “Num" are presented with dashed line and the Duden and Fottner (1997) experimental measurements labeled as “Exp", only available at $x/c_x = 1.50$, are presented with squares

is shown in Fig. 6, for which the calculations were performed by using a mass-averaging. It can be noticed that the two curves are very different from each other. The minimum value assumed by ω in C1 is always much smaller than that assumed in C2. Its percentage increase from the first case to the second one reaches values of around +300%. As far as the ω maximum is concerned, there is a trend reversal as the distance from the trailing edge grows: for $x/c_x = 1.03$ and $x/c_x = 1.10$ the maximum point in C1 is greater than in C2, whereas for $x/c_x = 1.30$ and $x/c_x = 1.50$ the ω positive peak in C2 becomes greater than in C1, with a percentage growth of about 15% for $x/c_x = 1.50$. Anyway, it is clear that the losses generated in C2 are averagely greater regarding those generated in C1 along the spanwise direction for all the axial locations. Regarding the comparison with the data available in literature, as mentioned for the flow angle β, also for ω the experimental measurements by Duden and Fottner (1997) and the numerical results by Marconcini *et al.* (2019) match fairly well the C2 curve.

The losses generated by the secondary flows can be analyzed also by plotting the 2D loss coefficient contours at various axial locations (Fig. 7). The pattern of the distribution shows the so

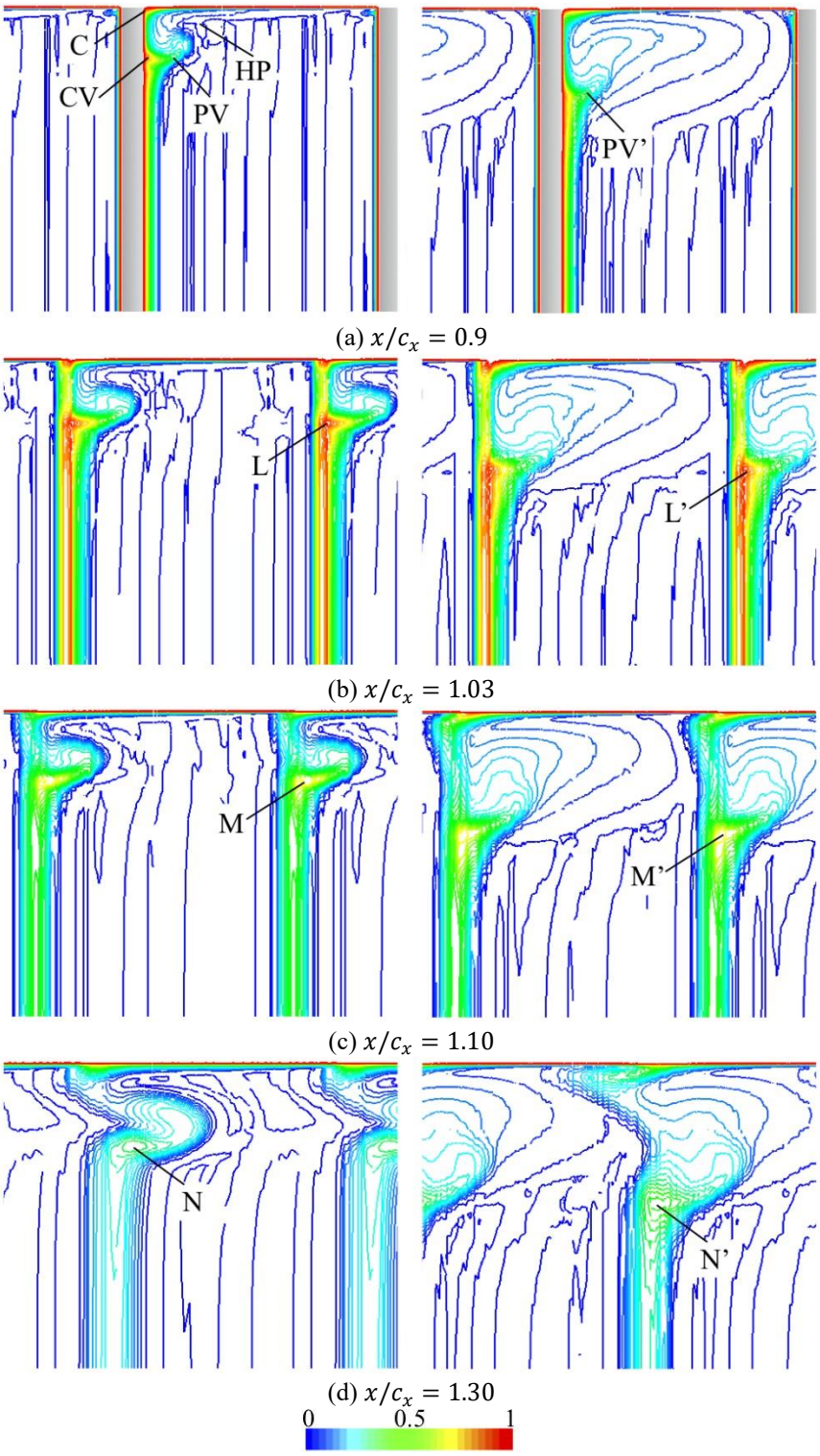

Fig. 7 Loss coefficient ω contours at four axial locations (left C1, right C2)

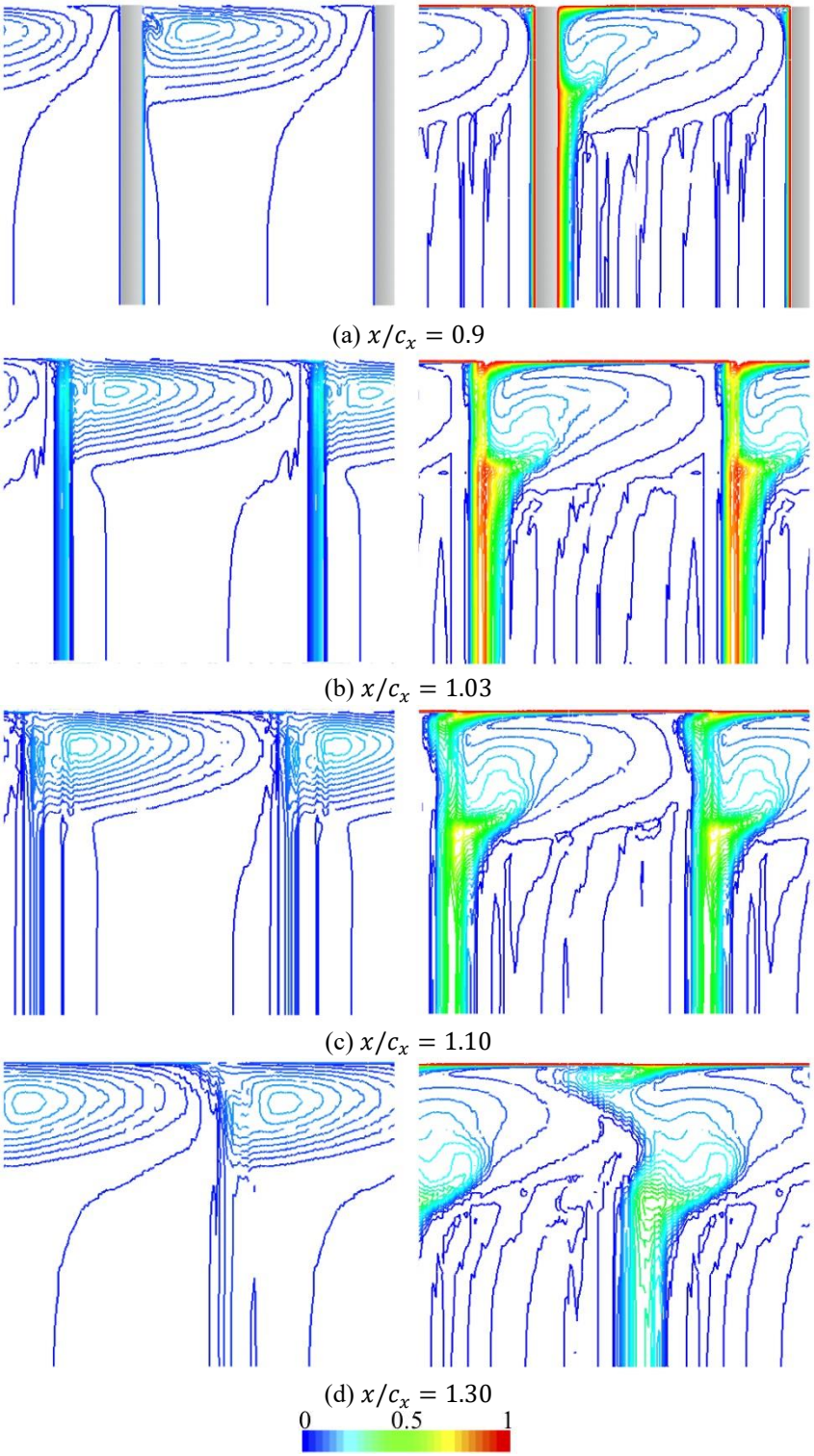

Fig. 8 Loss coefficient ω contours at four axial locations (left Euler, right C2)

called "dog-bone" geometry, typical for highly loaded turbine cascades. For $x/c_x = 0.9$ it is possible to distinguish the vortices which produces more losses, such as the passage vortex, the corner vortex, the pressure side leg of the horseshoe vortex and the counter vortex, indicated by the labels PV, C, HP and CV, respectively. The two cases show a very similar overall pattern, however it can be seen that in C2 losses are shifted towards the midspan plane and occupy a larger area in the pitchwise direction with respect to C1. In order to quantify this displacement, the distance between the passage vortex cores for C1 and C2 cases was measured, equal to $\Delta y/c_x = 0.12$. Additionally, at the axial locations $x/c_x = 1.10$, $x/c_x = 1.30$ e $x/c_x = 1.50$ the distance between points L and L', M and M', N and N' is equal to $\Delta y/c_x = 0.17$, $\Delta y/c_x = 0.20$, $\Delta y/c_x = 0.22$, respectively.

An analysis of Figs. 5, 6 and 7 reveals that for C2 the influence of secondary flows is present at further distances from the end-wall than C1 in the spanwise direction. While the secondary flows effects for the former can be notice up to almost one axial chord c_x from the end-wall, the effects of the latter can only be seen up to about half c_x.

4.5 Euler vs. RANS - C2

The main purpose of this section is to identify differences in the Euler and RANS C2 predictions of secondary flows in order to estimate the influence of viscosity and turbulence on the end-wall flow field. As already mentioned, the horseshoe vortex generation is an inviscid phenomenon, as long as a flow velocity gradient is present near the end-wall. For this reason, the simulation that solves the Euler equations was conducted by imposing an inlet boundary layer. Without it, the flow would have been completely two-dimensional with velocity component in the spanwise direction equal to zero at every point of the domain.

With reference to Fig. 8, which shows the loss coefficient ω contours at different axial locations, it can be seen that the losses estimated from Euler equations are well localized and confined to the only region of the domain where secondary flows vorticity dominates. In contrast to RANS, the cascade passage simulated solving Euler equations is mainly governed by a single large and homogeneous vortex structure, whose core does not move away from the end-wall proceeding downstream of the trailing edge.

Analyzing Fig. 9 illustrating the pitchwise averaged flow angle β along the spanwise direction for Euler and C2 cases, it is visible that the Euler inviscid flow experiences an important variation of pitchwise direction along the spanwise direction immediately downstream the blade trailing edge as well. The difference between the maximum value assumed by β for Euler and C2 cases is practically negligible, however in the end-wall proximity the Euler case does not show a real overturning phenomena, since at $\hat{y}/H = 0$ the flow does not have zero velocity and is already oriented by the maximum angle. On the contrary, the underturning peak is quite different: for C2 curve it is much greater and further from the end-wall than for Euler curve. Furthermore, the two distributions asymptotically reach the same value as expected, as away from the end-wall and blade the compressible field tends to incompressible.

Finally, in Fig. 10 is shown the pressure distribution around the blade at different spanwise locations $\hat{y}/H$, for RANS and Euler results. It is observed as the Euler curve is always under the C2 curve due to the absence of the boundary layer on the blade. However, at the end-wall ($\hat{y}/H = 0$), where the flow field is dominated by the effect of secondary flows vorticity, the two distributions are essentially overlapping. In proximity of the trailing edge of the blade, for all the investigated spanwise positions, it is possible to observe some pressure oscillations in the Euler

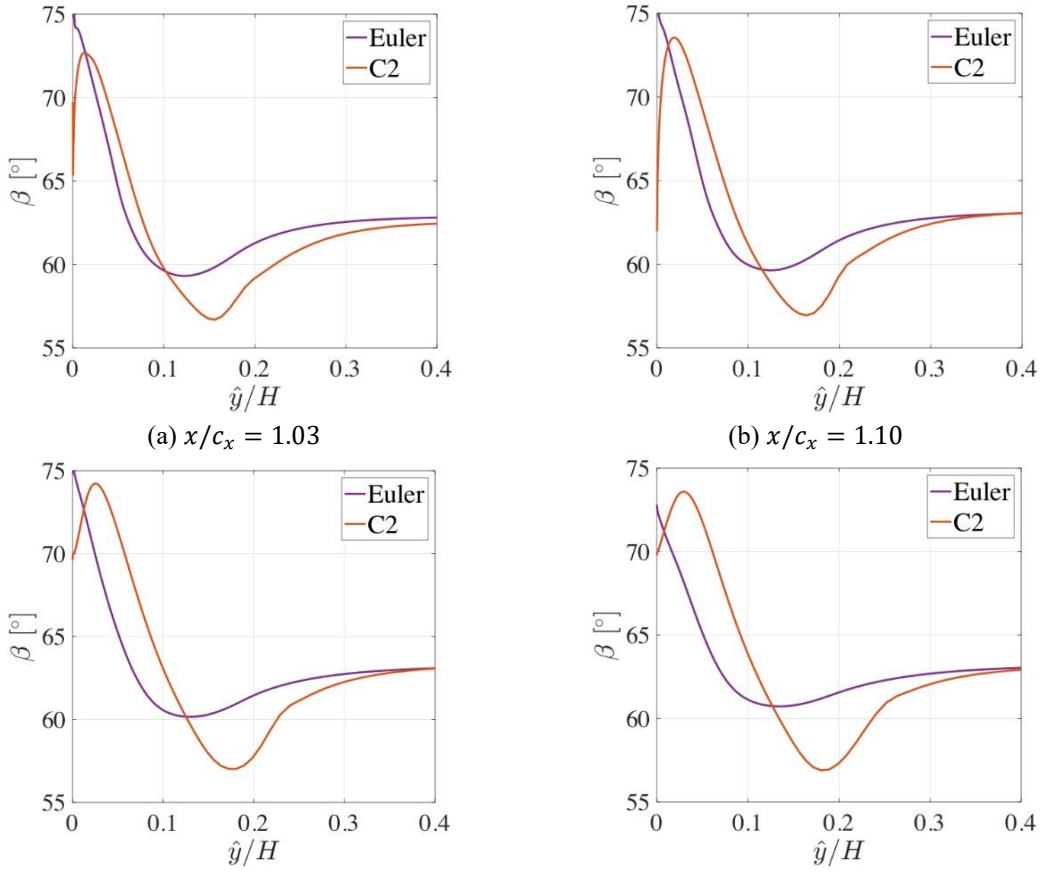

(a) $x/c_x = 1.03$ (b) $x/c_x = 1.10$

(c) $x/c_x = 1.30$ (d) $x/c_x = 1.50$

Fig. 9 Comparison of the pitchwise averaged flow angle β respect to the axial direction, obtained by solving Euler and RANS equations, along the spanwise direction at four axial locations

results. These oscillations are related to the development of a weak shock wave close to the trailing edge when the inviscid flow is considered: since the discretization adopted in this work does not include artificial viscosity or other shock capturing techniques these oscillations are expected but limited to the trailing edge region.

5. Conclusions

The flow field within the T106A linear cascade has been studied to examine the secondary flows details. This investigation aims at two main objectives. First of all two different inlet conditions have been inspected with RANS, inlet boundary layer and inlet uniform conditions, in order to explore the influence of incoming boundary layer over the end-wall flow field. It has been observed that the presence of an inlet boundary layer profile has a significant impact on the cascade flow field. Compared to the inlet uniform conditions case, the one with the inlet boundary layer has been found to be characterized by pronounced secondary flows structures. This can be

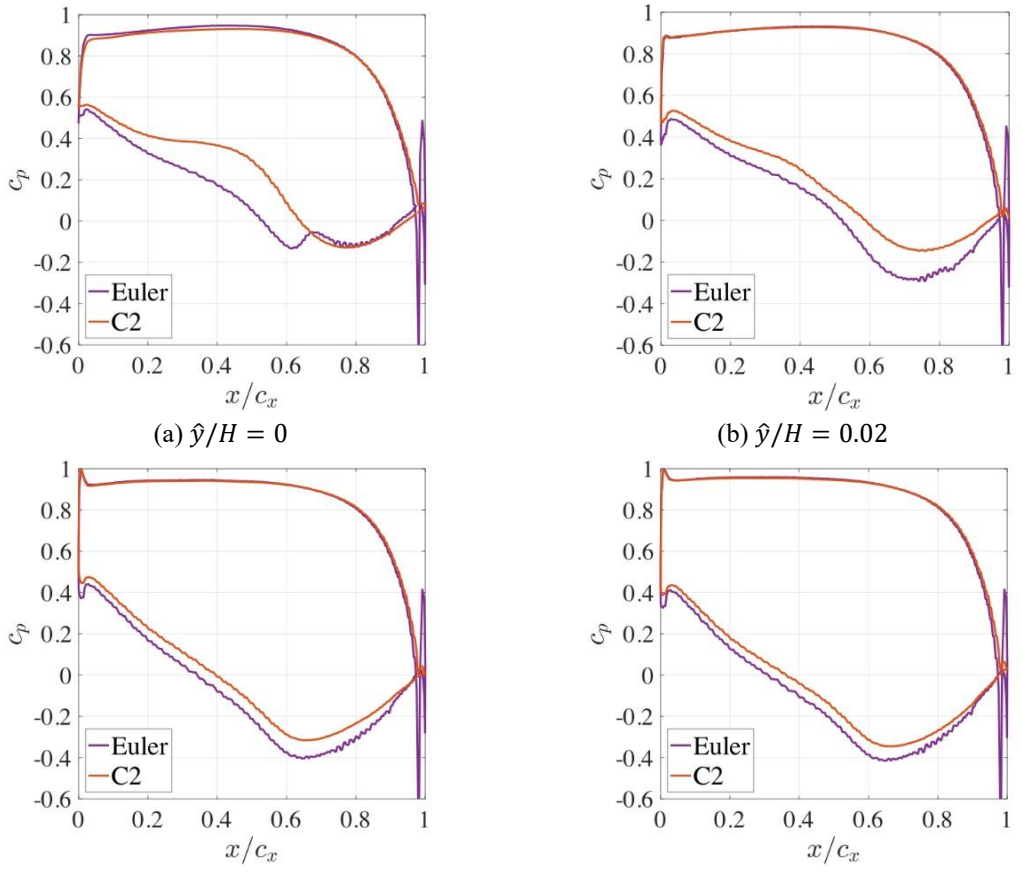

(a) $\hat{y}/H = 0$ (b) $\hat{y}/H = 0.02$

(c) $\hat{y}/H = 0.15$ (d) $\hat{y}/H = 0.50$

Fig. 10 Pressure distribution around the blade at different spanwise locations $\hat{y}/H$. The results obtained by solving Euler and RANS equations are compared

seen in the evolution of streamlines along the passage, loss of lift close to the end-wall, greater over turning and under turning angles, higher and more extended in space total pressure losses. In addition, it is noted that the influence of secondary flows is present up to a greater distance from the end-wall due to the inlet boundary layer. Furthermore, comparisons with experimental (Duden and Fottner 1997) and numerical (Pichler *et al.* 2019, Marconcini *et al.* 2019) data available in literature showed good agreement.

The second goal of the present work was to estimate the influence of viscosity and turbulence on the end-wall flow field. For this reason an additional simulation which solves the Euler equations was conducted by imposing the same inlet boundary layer used for the former RANS analysis. The results obtained are globally comparable, although they present evident differences. The cascade passage simulated with inviscid flow is mainly dominated by a single large and homogeneous vortex structure, less stretched in the spanwise direction and closer to the end-wall than the aerodynamic structures resulting from the compressible flow simulation.

Findings showed that for the chosen cascade with the Reynolds number and Mach number combination employed, a great part of the secondary flows details is strongly dependent on

viscous phenomena. Therefore, the selection of the parameters with which to perform the RANS analysis and the choice of turbulence model are undoubtedly crucial to simulate the end-wall flow field for the present test-case. In this regard, it is emphasized that the comparisons made with the experimental and numerical data available in literature have demonstrated that Spalart-Allmaras offers excellent results, considering that it is computationally cheaper than the model used by Pichler *et al.* (2019), Marconcini *et al.* (2019).

Acknowledgments

Computational resources provided by hpc@polito, which is a project of Academic Computing within the Department of Control and Computer Engineering at the Politecnico di Torino (http://www.hpc.polito.it).

References

Allmaras, S., Johnson, F. and Spalart, P. (2012), "Modifications and clarifications for the implementation of the Spalart-Allmaras turbulence model", *Seventh International Conference on Computational Fluid Dynamics (ICCFD7)*, Big Island, Hawaii, July.

Balay, S., Gropp, W.D., McInnes, L.C. and Smith, B.F. (1997), "Efficient management of parallelism in object-oriented numerical software libraries", *Modern Software Tools for Scientific Computing*, Birkhäuser Boston, Boston, MA, United States.

Cui, J., Rao, V.N. and Tucker, P.G. (2017), "Numerical investigation of secondary flows in a high-lift low pressure turbine", *Int. J. Heat Fluid Flow*, **63**, 149-157. https://doi.org/10.1016/j.ijheatfluidflow.2016.05.018.

de la Blanco, E.R., Hodson, H., Vazquez, R. and Torre, D. (2003), "Influence of the state of the inlet endwall boundary layer on the interaction between pressure surface separation and endwall flows", *Proc. Inst. Mech. Eng., Part A: J. Power Energy*, **217**(4), 433-441. https://doi.org/10.1243/095765003322315496.

Duden, A. and Fottner, L. (1997), "Influence of taper, Reynolds number and Mach number on the secondary flow field of a highly loaded turbine cascade", *Proc. Inst. Mech. Eng., Part A: J. Power Energy*, **211**(4), 309-320. https://doi.org/10.1177/095765099721100401.

Errante, M., Ferrero, A. and Larocca, F. (2022), "Simulation of secondary flows in turbomachinery by the discontinuous Galerkin method", *AIP Conf. Proc.*, **2611**, 050005. https://doi.org/10.1063/5.0120392.

Ferrero, A., Larocca, F. and Puppo, G. (2015), "A robust and adaptive recovery-based discontinuous Galerkin method for the numerical solution of convection-diffusion equations", *Int. J. Numer Meth. Fluid.*, **77**(2), 63-91. https://doi.org/10.1002/fld.3972.

Garai, A., Diosady, L.T., Murman, S.M. and Madavan, N.K. (2017), "Scale-resolving simulations of bypass transition in a high-pressure turbine cascade using a spectral element discontinuous Galerkin method", *J. Turbomach.*, **104**(3), 031004. https://doi.org/10.1115/1.4038403.

Geuzaine, C. and Remacle, J.F. (2009), "Gmsh: A three-dimensional finite element mesh generator with built-in pre- and post-processing facilities", *Int. J. Numer. Meth. Eng.*, **79**(11), 1309-1311. https://doi.org/10.1002/nme.2579.

Ghidoni, A., Colombo, A., Rebay, S. and Bassi, F. (2013), "Simulation of the transitional flow in a low pressure gas turbine cascade with a high-order discontinuous Galerkin method", *J. Fluid. Eng.*, **135**(7), 071101. https://doi.org/10.1115/1.4024107.

Giuliani, A. (2022), "A two-dimensional stabilized discontinuous galerkin method on curvilinear embedded boundary grids", *SIAM J. Scientif. Comput.*, **44**(1), A389-A415. https://doi.org/10.1137/21M1396277.

Goldstein, R. and Spores, R. (1988), "Turbulent transport on the endwall in the region between adjacent turbine blades", *J. Heat Transf.*, **110**(4a), 862-869. https://doi.org/10.1115/1.3250586.

Gulizzi, V., Almgren, A.S. and Bell, J.B. (2022), "A coupled discontinuous Galerkin-Finite Volume framework for solving gas dynamics over embedded geometries", *J. Comput. Phys.*, **450**, 110861. https://doi.org/10.1016/j.jcp.2021.110861.

Langston, L. (1980), "Crossflows in a turbine cascade passage", *J. Eng. Power*, **102**(4), 866-874. https://doi.org/10.1115/1.3230352.

Langston, L. (2001), "Secondary flows in axial turbines-A review", *Ann. NY Acad. Sci.*, **934**(1), 11-26. https://doi.org/10.1111/j.1749-6632.2001.tb05839.x.

Lax, P.D. (1954), "Weak solutions of nonlinear hyperbolic equations and their numerical computation", *Commun. Pure Appl. Math.*, **7**, 159-193. https://doi.org/10.1002/cpa.3160070112.

LeVeque, R. (2002), *Finite Volume Methods for Hyperbolic Problems*, Cambridge University Press, Cambridge, United Kingdom.

Lo, M. and van Leer, B. (2009), "Analysis and implementation of recovery-based discontinuous Galerkin for diffusion", *19th AIAA Computational Fluid Dynamics*, San Antonio, Texas, June. https://doi.org/10.2514/6.2009-3786.

Marconcini, M., Pacciani, R., Arnone, A., Michelassi, V., Pichler, R., Zhao, Y. and Sandberg, R. (2019), "Large eddy simulation and RANS analysis of the end-wall flow in a linear low-pressure-turbine cascade-part II: Loss generation", *J. Turbomach.*, **141**(5), 051004. https://doi.org/10.1115/1.4042208.

Pandolfi, M. (1984), "A contribution to the numerical prediction of unsteady flows", *AIAA J.*, **22**(5), 602-610. https://doi.org/10.2514/3.48491.

Pichler, R., Zhao, Y., Sandberg, R., Michelassi, V., Pacciani, R., Marconcini, M. and Arnone, A. (2019), "Large-eddy simulation and RANS analysis of the end-wall flow in a linear low-pressure turbine cascade, Part I: Flow and secondary vorticity fields under varying inlet condition", *J. Turbomach.*, **141**(12), 121005. https://doi.org/10.1115/1.4045080.

Rusanov, V.V. (1962), "The calculation of the interaction of non-stationary shock waves and obstacles", *USSR Comput. Math. Math. Phys.*, **1**(2), 304-320. https://doi.org/10.1016/0041-5553(62)90062-9.

Sieverding, C. (1985), "Recent progress in the understanding of basic aspects of secondary flows in turbine blade passages", *J. Eng. Gas Turbin. Power*, **107**(2), 248-257. https://doi.org/10.1115/1.3239704.

Sieverding, C. and Van Den Bosche, P. (1983), "The use of coloured smoke to visualize secondary flows in a turbine-blade cascade", *J. Fluid Mech.*, **134**, 85-89. https://doi.org/10.1017/S0022112083003237.

Wang, H., Olson, S., Goldstein, R. and Eckert, E. (1997), "Flow visualization in a linear turbine cascade of high performance turbine blades", *J. Turbomach.*, **119**(1), 1-8. https://doi.org/10.1115/1.2841006.

Yao, M. and He, L. (2012), "Implicit discontinuous Galerkin solution on unstructured mesh for turbine blade secondary flow", *J. Turbomach.*, **142**(1), 011004. https://doi.org/10.1115/1.4045551.